Combining Magnetic Particle Imaging and Magnetic Fluid Hyperthermia in a Theranostic Platform

Daniel Hensley[1,*], **Zhi Wei Tay**[1], **Rohan Dhavalikar**[2], **Bo Zheng**[1], **Patrick Goodwill**[3], **Carlos Rinaldi**[2,4], and **Steven Conolly**[1,5]

[1]Department of Bioengineering, University of California Berkeley, USA

[2]Department of Chemical Engineering, University of Florida, Gainesville, USA

[3]Magnetic Insight, Inc., Alameda, CA, USA

[4]Department of Biomedical Engineering, University of Florida, Gainesville, USA

[5]Department of Electrical Engineering and Computer Sciences, University of California, Berkeley, USA

Abstract

Magnetic particle imaging (MPI) is a rapidly developing molecular and cellular imaging modality. Magnetic fluid hyperthermia (MFH) is a promising therapeutic approach where magnetic nanoparticles are used as a conduit for targeted energy deposition, such as in hyperthermia induction and drug delivery. The physics germane to and exploited by MPI and MFH are similar, and the same particles can be used effectively for both. Consequently, the method of signal localization by using gradient fields in MPI can also be used to spatially localize MFH, allowing for spatially selective heating deep in the body and generally providing greater control and flexibility in MFH. Furthermore, MPI and MFH may be integrated together in a single device for simultaneous MPI-MFH and seamless switching between imaging and therapeutic modes. Here we show simulation and experimental work quantifying the extent of spatial localization of MFH using MPI systems: We report the first combined MPI-MFH system and demonstrate on-demand selective heating of nanoparticle samples separated by only 3 mm (up to 0.4 C/s heating rates and 150 W/g SAR deposition). We also show experimental data for MPI performed at a typical MFH frequency and show preliminary simultaneous MPI-MFH data.

1. Introduction and Background

While anatomical imaging modalities such as X-ray computed tomography (CT) and magnetic resonance imaging (MRI) are staples of clinical medicine, many pathologies such as cancer may not be readily perceived in such images, especially in early and critical stages of the disease (Etzioni et al. 2003; Serres et al. 2012; Li 2014). Physiologic contrast between healthy and pathological tissue is needed in these cases. Molecular imaging modalities such as magnetic particle imaging (MPI) can provide this valuable physiologic and functional

---

*dwhensley@berkeley.edu.

information in a clinical context (James and Gambhir 2012; Pablico-Lansigan, Situ, and Samia 2013).

Imaging and other diagnostics are ultimately combined with some interventional therapy to treat disease. Combining both aspects into a single "theranostic" platform can deliver faster, more flexible, and more precise treatment and ultimately improve patient outcomes. Real-time interactions and feedback between the diagnostic imaging and therapeutic components can lead to enhanced functionality. For example, recent work combining positron emission tomography (PET) and radiation therapy has led to the development of Emission Guided Radiation Therapy (EGRT), which may improve radiation treatment targeting (Fan et al. 2012). More traditionally, oncologists and radiation therapists use separate PET/CT to target subsequent radiation therapy.

An ideal theranostic imaging platform would be noninvasive, safe, and provide fully real-time feedback. We believe such a platform can be provided by the union of MPI and magnetic fluid hyperthermia (MFH). MPI is a new imaging modality that has been established as both a preclinical vascular tracer modality and a preclinical molecular and cellular imaging modality (Jörn Borgert et al. 2012; Zheng, Vazin, et al. 2015; Zheng, See, et al. 2016). MFH is a method of heating nanoparticles by driving them through their nonlinear magnetization curve. MPI has the potential to provide *both* imaging and MFH treatment in real-time.

The magnetization curves of magnetic nanoparticles used in MPI and MFH are characterized by a nonlinear saturation at high field magnitudes. As illustrated in Fig. 1 and Fig. 2, gradient fields saturate the nanoparticles everywhere except in the vicinity of a field-free region (FFR) created by the gradients. In the saturated regions, the particles are effectively locked in place and neither an appreciable MPI signal nor heating occur in response to an AC excitation field. We and other groups have been actively exploring the ramifications of MPI and gradient fields in MFH (Tasci et al. 2009; Khandhar et al. 2012; Murase, Takata, et al. 2013; Murase, Aoki, et al. 2015; Kuboyabu et al. 2016; Maruyama et al. 2016; Bauer et al. 2016; Behrends, Buzug, and A. Neumann 2016).

Here we describe the construction of a combined MPI-MFH scanning system, which we use to explore and quantify the possibilities of an MPI theranostic system. We show that standard MPI hardware can guide MFH treatments to any desired region within a subject, providing actuation with high spatial resolution as well as seamless switching between imaging and therapy while the subject remains in the scanner.

1.1. Magnetic Particle Imaging

MPI is an emerging tracer-based molecular imaging modality, first described in 2005 (Bernhard Gleich and Jurgen Weizenecker 2005). Soon after, important work elaborating on the MPI signal equations and 3D *in vivo* applications of the system matrix method were developed (Rahmer et al. 2009; J Weizenecker et al. 2009) as well as the description of the x-space approach to MPI (Goodwill and Conolly 2010; Goodwill and Conolly 2011; Saritas et al. 2013). MPI uses magnetic fields to detect superparamagnetic iron oxide (SPIO) tracers present in an imaging field of view (FOV). Strong magnetic field gradients are used to create

a sensitive FFR delineated from an encompassing region of high magnetic field magnitude. To scan a FOV, spatially homogeneous but temporally varying excitation and shift fields are superposed on the gradient field and/or mechanical means of shifting the excitation magnets and sample are employed. The result is to shift the position of the FFR relative to the object of interest. The fast excitation induces the bulk of the received signal while the shift mechanisms allow coverage of a large FOV over time. In some approaches, fast excitation concomitantly in multiple directions can allow encoding of data in a FOV quickly without the use of any distinct slow shift mechanisms (B Gleich, J Weizenecker, and J Borgert 2008). In designing MPI systems and choosing the excitation strategy, tradeoffs between parameters such as image acquisition speed, total FOV size, and SNR are inherent.

Regardless of the details of the trajectory, due to the nonlinear saturation magnetization that defines SPIO tracers, only when the FFR is coincident with a region containing tracer will a significant change in the tracer magnetization be induced by the AC excitation field. When the FFR is farther away, the tracer is saturated and no signal is detected because there is no appreciable change in SPIO magnetization. The basics of our MPI acquisition and reconstruction approach are depicted in Fig. 1.

Signal acquisition may be thought of as direct sampling of the spatial domain using a translating sensitive region. Inductive pickup coils are used to record the changes in magnetization over time. Image reconstruction involves a mapping of the time-domain signal to a regular grid in the image domain using knowledge of the FFR trajectory. Intermediate steps such as compensation for the changing velocity of the AC excitation and recovery of information lost due to direct feedthrough mitigation strategies are described in our prior work (K. Lu et al. 2013; Konkle, Goodwill, Hensley, et al. 2015). Reconstruction may also be formulated as an inverse problem by measuring system functions and constructing a suitable system matrix (Rahmer et al. 2009; Rahmer et al. 2012). Per the saturation physics described in Fig. 1, both of these reconstruction methods report resolution that scales inversely with the gradient strength (Rahmer et al. 2009; Goodwill and Conolly 2010).

MPI has been used in several *in vivo* application domains to date, including cell tracking (Zheng, Vazin, et al. 2015; Zheng, See, et al. 2016), cancer imaging (Yu et al. 2016), blood pool and perfusion imaging (Orendorff et al. 2016), angiography and cardiac imaging (J Weizenecker et al. 2009), lung ventilation and perfusion studies (Nishimoto et al. 2015; Zhou et al. 2016), and predicting the effect of MFH (Kuboyabu et al. 2016). These results highlight the strengths of MPI: zero background signal, zero depth attenuation of the signal, high sensitivity, linear quantification, and no half-life associated with the tracer signal such that physiologic clearance times determine the time horizons available in longitudinal studies. For example, we previously showed the ability to detect fewer than 200 labeled stem cells and *in vivo* cell tracking over a period of time exceeding 80 days (Zheng, Vazin, et al. 2015; Zheng, See, et al. 2016).

1.2. Magnetic Fluid Hyperthermia

Magnetic fluid hyperthermia (MFH) encompasses an array of therapeutic approaches that use magnetic nanoparticles (MNPs) to couple magnetic energy into the body to heat

diseased tissue (Jordan, Scholz, Peter Wust, et al. 1999; Rosensweig 2002; Jordan, Scholz, Maier-Hauff, et al. 2006; Thiesen and Jordan 2008). Direct hyperthermia and tissue ablation that rely on large temperature changes have been studied in applications such as cancer treatment (Hilger et al. 2002; Manfred Johannsen et al. 2010; Branquinho et al. 2013). For tissue ablation therapies, a typical goal is to heat a target tissue region to above 43 $°C$ to achieve the desired effect. However, heat-induced cell death is generally a complex function of time and temperature, motivating the use of more heuristic assessments. For example, the nonlinear metric cumulative equivalent minutes at 43 $°C$ (CEM_{43}) establishes a thermal dose for any time-temperature trajectory that tissue is subjected to (Sapareto and Dewey 1984; Dewhirst et al. 2003; Dewey 2009). In this context, a goal such as $CEM_{43} = 240$ may be sought in the region of interest.

Other therapeutic techniques require increasing temperature by only a few degrees. For example, limited or mild *hyperthermia* therapy in conjunction with chemotherapy or radiation therapy has been explored as a way to enhance therapeutic potency (Torres-Lugo and Rinaldi 2013; Maier-Hauff et al. 2011). More recently, research has indicated that no macroscopic temperature change may be necessary to induce cell death in targeted tissues (Creixell et al. 2011; Domenech et al. 2013). Additionally, MFH may be leveraged for drug delivery through, for example, selective breaking of thermally labile bonds or use of thermally-dependent permeabilities without detectable macroscopic temperature changes (Kumar and Mohammad 2011; Zhang and Misra 2007).

1.3. Spatial targeting of MNPs and MFH

Spatially targeting MFH therapies is a primary concern of the technique. There are two ways to spatially target the effects of MFH: targeting the tracer and targeting the energy deposition. We discuss both approaches separately.

Targeting the tracer—MFH intrinsically provides spatial localization of the therapy via the distribution of the MNPs. A major challenge in MFH is ensuring high enough concentrations of MNPs at target sites to effect significant macroscopic temperature changes. Accordingly, many *in vivo* pre-clinical and clinical studies to date have used direct intratumoral injection of tracer in lieu of effective active targeting mechanisms following systemic injection (Manfred Johannsen et al. 2010). In general, the required concentration is a function of the MNP properties, heat transfer conditions, and magnetic field parameters. It has been reported that 5 milligrams ferrite per gram of tumor, or approximately 5 $mg\ mL^{-1}$ MNP concentration, is suitable for MFH using clinically acceptable magnetic field excitation conditions (Jordan, P Wust, et al. 2009). In one *in vivo* human trial to treat prostate cancer, the authors report direct injection of 12.5 mL of 120 $mg\ mL^{-1}$ MNP solution (injected in smaller volumes at 24 different locations) into a 35 mL prostate (M Johannsen et al. 2005). Assuming uniform distribution, that all of the injected MNP fluid remained in the prostate, and summing the injected and prostate volumes, we calculate that up to approximately 30 $mg\ mL^{-1}$ MNP concentration was achieved in the target lesion. With these concentrations, temperatures in excess of 48 $°C$ were achieved in the lesion using MFH.

A longer term goal is to leverage various *in vivo* MNP targeting mechanisms such that the therapy may be localized by the distribution of the particles following systemic introduction. However, high specificity targeting of nanoparticles and small molecules is still an open problem. Regardless of the method of introduction, MNPs will to some degree make their way into non-target regions such as the liver. An ability to robustly and reliably target only those MNPs associated with a therapeutic region is an important ultimate requirement for any clinical MFH approach.

Spatially Controlled Heating—Our ability to focus electromagnetic fields at the frequencies used in MFH (around 300 kHz) is fundamentally limited by diffraction, regardless of the number of external coils employed, to about half the *in vivo* wavelength. Unfortunately, at 300 kHz, this value is roughly 50 meters and much larger than the subject. Many MFH methods use large homogeneous field-producing coils as illustrated in Fig. 2(a). This leads to significant heat deposition at all sites where the MNP concentration is high, including healthy sites of accumulation. Alternatively, surface coils which do not provide a homogeneous excitation field can be used to target the heating, as depicted in Fig. 2(b). Due to the rapid decay of the magnetic field with distance from the coil, this approach can selectively target lesions near the surface of the subject, but it cannot deliver energy to particle distributions deeper in the body. There is currently no way in MFH to target specific regions of accumulated magnetic nanoparticles arbitrarily deep in the body. This is a serious clinical challenge since the non-specific uptake of even targeted MNPs is far higher in the excretory organs (liver, spleen, or kidneys) than in the targeted region (Wilhelm et al. 2016).

The use of a strong magnetic field gradient can potentially solve MFH spatial targeting, as illustrated in Fig. 2(c). A strong DC field fully saturates MNPs, locking them into alignment. An AC excitation field is then unable to induce a rotation, which is required to generate heating. With an MPI gradient system in place, heating will be isolated to the FFR – the only location where MNPs are unsaturated. The spatial resolution of heating should scale similarly to the MPI spatial resolution since the localization mechanism is identical. In this manner, an MPI-MFH system can provide targeted heating with high resolution arbitrarily deep in the body.

1.4. Combining MPI-MFH

Combining MPI and MFH could lead to even greater gains than spatially targeted MFH by providing real-time feedback for more refined and safe therapy. Murase et al. recently showed that MPI can be used to predict the effect of subsequent MFH due to the common physics that generates the MPI signal and MFH heating (Murase, Aoki, et al. 2015). Combined MPI-MFH could enable continuous monitoring of tumor position, real-time quantitation of SAR deposition or temperature (Weaver, Rauwerdink, and Hansen 2009), and real-time assessment of treatment success. In this context, rigorous quantitation may require accounting for the effects of magnetic relaxation on the MPI signal and MFH therapy. For example, it is known that the MPI signal is affected by the excitation amplitude due to magnetic relaxation dynamics (Croft et al. 2016), and binding events when using targeted tracers may also change the nature of the signal.

Such real-time or simultaneous approaches are in contrast to current MFH approaches that are open-loop or require invasive temperature probes, complex pre-planning heating simulations, or provide only limited imaging feedback (Laurent et al. 2011). In this paper, we demonstrate a unified MPI-MFH system that may one day solve the problem of high resolution localization of MFH while providing seamless and non-invasive feedback *in vivo*.

2. Materials and Methods

In this work, a combined MPI-MFH system was built and several MPI systems previously built by our group were used. Simulations based on recent MFH models, modified to include the presence of gradient fields, were also performed.

2.1. MPI-MFH System

A field-free line (FFL) based combined MPI-MFH system was constructed with a 2.35 T/m gradient provided by a quadrupole NdFeB magnet array oriented around a cylindrical imaging bore as shown in Fig. 3(a) and Fig. 4(a) (Goodwill, Konkle, et al. 2012; Konkle, Goodwill, Carrasco-Zevallos, et al. 2013). A solid copper shield defines the imaging bore in which concentric solenoidal excitation (Tx) and MPI receive (Rx) coils were placed. A simple resonant filter chain was implemented as shown in Fig. 3(b), consisting of an initial impedance matching and low pass filter component and final resonant stage connected to the Tx coil. This system is resonant at $f_0 = 353$ kHz with an optimal real input impedance of 50 ohms seen by the power amplifier at f_0. A Tomco BT00500-AlphaS-CW amplifier (Tomco Technologies, South Australia) was used to power the system. This setup allowed for up to 20 mT excitation across a 95% homogeneity region of approximately 2 cm. A sample delivery and movement system was constructed using linear stages driven by stepper motors in all three principal axes. In this manner, the position of a 3D-printed sample holder can be controlled precisely to realize desired MFH or MPI-MFH scan trajectories coded in MATLAB (MathWorks, MA, USA) scripts. All MFH and MPI-MFH scans using this system were taken in a one dimensional format, with relative movement between the sample and FFL confined along the axis of the cylindrical imaging bore and solenoidal Tx/Rx coils. This is the "z" axis by our convention.

As in our previous MPI systems, the Tx coil was wound using hollow-core copper wire. A room temperature hydraulic circuit for cooling was installed inline with the coil to allow Joule heating of the coil to be removed without confounding the MPI-MFH experiments. A Gaymar T/Pump controlled temperature and pump system (Stryker Corporation, Kalamazoo, MI, USA) powered the cooling circuit, providing 0.5 liters per minute flow of room temperature water.

For MFH data acquisition, temperature data was collected using optical temperature probes designed for safe use in magnetic systems (Neoptix, Canada). These small probes were placed directly in contact with the tracer fluid in phantom vials containing MNPs in aqueous solution. Temperature data from these probes was sampled at 10 Hz using a MATLAB script and a standard serial communication interface.

For MPI data acquisition, an MPI Rx coil wound in a gradiometric fashion was placed internally concentric with the transmit coil as depicted in Fig. 3(a). As is standard in MPI, to maximize dynamic range in the receive chain, this coil was physically tuned for maximum cancellation of the transmit feedthrough that couples into the Rx coil due to the mutual inductance of the Tx and Rx coils. A second phase sniffer coil was also placed in the imaging bore to calibrate relative phase between the transmit and receive systems and ensure phase coherence in MPI analysis and reconstruction. The basic receive chain consisted of an SR560 low noise voltage preamplifier (Stanford Research Systems, Inc., CA, USA), and the raw data was sampled at 10 MHz using a PCI-6115 12-bit ADC (National Instruments, TX, USA). A Python script was used to analyze ID MPI data.

To characterize the Tx coil and calibrate the input voltage to output field relationship, a Fluxtrol Magnetic AC field probe (Fluxtrol Inc., MI, USA) was used. To characterize the gradient field, a Lake Shore DSP 475 DC field probe (Lake Shore DSP, OH, USA) was used. These probes were placed in the sample holder and moved through the imaging bore using the linear stage and motor system for precise calibration.

2.2. MPI-MFH Experiments

Several types of MPI-MFH experiments were performed, all with phantoms constructed using samples of nanoMag-MIP SPIOs (78-00-102, micromod Partikeltechnologie GmbH, Rostock, Germany) as shown in Fig. 4(d) (Eberbeck et al. 2013). These particles are polydisperse SPIOs coated with dextran (total hydrodynamic diameter in the range of 20 – 100 nm) and are similar to Ferucarbotran (Resovist) used widely in the MPI field. In some experiments, a single vial of nanoMag MIP (100 μL at 10.6 $mg\ mL^{-1}$. iron) tracer was placed in the sample holder, and an MFH sequence' was applied using 20 mT excitation applied for 10–60 s with the sample fixed at a, single position relative to the FFL. The 10.6 $mg\ mL^{-1}$ is similar to clinically relevant MFH concentrations described in the literature (Jordan, P Wust, et al. 2009; M Johannsen et al. 2005). This procedure was repeated after the sample was moved along the axis of the bore to sample the MFH signal as a function of position in one dimension. Replicate experiments were carried out to assess repeatability and report statistical variation.

In other experiments, the ability for repeatable and precise spatial selection in MFH was tested directly with a phantom containing three nanoMag MIP vials (each 100 μL at 10.6 $mg\ mL^{-1}$ iron) separated from each other by 3 mm (7 mm center-to-center distance). In some actuation sequences, a specific vial was individually targeted for heating while in others, each vial was targeted for heating in rapid succession. Replicate experiments were carried out to assess repeatability and report statistical variation.

In a third set of experiments, simultaneous MFH and MPI was performed. The setup and trajectory were the same as reported above (single nanoMag MIP vial actuated at different points along the imaging bore), but MPI data was recorded. Data was also taken for a PBS control subjected to the same scan trajectory. In analyzing the MPI signal, baseline removal was performed using the control data and linear baseline subtraction.

The imaging phantom used in MPI-MFH experiments was also separately imaged in MPI-only devices to assess the quality of the phantoms in standard MPI. The field-free point (FFP) scanner shown in Fig. 4(b) was used for multi-dimensional MPI imaging of the phantoms. This scanner has a $3.5 \times 3.5 \times 7$ $T\,m^{-1}$ gradient system with excitation at $f_0 = 20$ kHz and up to 30 mT. An amplitude of 20 mT was used in this work. Full 3D tomographic data sets took approximately 10 minutes to acquire and reconstruct.

In addition to the MPI-MFH and MPI-only experiments, the nanoMag MIP sample vials were also tested on our arbitrary waveform relaxometer (AWR) system. This tabletop system has no gradient fields. Instead, a sinusoidal excitation and linear bias field are superposed to test the aggregate response of a sample in the applied magnetic field space (Tay et al. 2016). This system can reconstruct 1D MPI point-spread functions (PSFs) (Croft et al. 2016; Tay et al. 2016). The AWR was used to test the quality of MPI at the higher frequencies used in MFH. Experiments were run with $f_0 = 353$ kHz to match the MPI-MFH system and an excitation amplitude of 2 mT.

2.3. Simulation

Simulations were carried out to predict the response of particles to AC fields in the presence of a static magnetic field gradient. The simulations were based on the theoretical model developed by Dhavalikar and Rinaldi (Dhavalikar and Rinaldi 2016) which was constructed using the magnetization relaxation equation described by Martsenyuk et al. (Martsenyuk, Raikher, and Shliomis 1974) to calculate heat dissipation as specific absorption rate (SAR). SAR values are calculated directly from a thermodynamic model wherein the work done by an applied magnetic field on the particles is dissipated as heat.

The nanomag-MIP particles primarily consist of 19 nm core particles. These cores are arranged as clusters in dextran with hydrodynamic diameters in the range of 20–100 nm (Eberbeck et al. 2013). In simulation, an iron oxide domain magnetization of 446 $k\,Am^{-1}$ (Rosensweig 2013) and density of 5.18 $g\,cm^{-1}$ were used (Narasimha, Brennan, and Holtham 2006; Rosensweig 2002). The thickness of the dextran shell was varied to obtain SAR values comparable to those in the experiments. Interparticle interactions were not included in the model. For an aqueous solution at room temperature, as in the experiments, a viscosity of 0.89 $mPa \cdot s$ and temperature of 298 K were assumed. Simulations were carried out an excitation amplitude of 20 mT and an excitation frequency of 353 kHz to match the experimental setup. To assess the effect of field gradient on the spatial distribution of SAR, simulations were performed with MPI field gradients in the range of 1–7 $T\,m^{-1}$ based on gradient strengths typically encountered in existing MPI scanners.

2.4. SAR Calculations

To calculate experimental SAR, a commonly used approximate method (Murase, Takata, et al. 2013) based on a linear fit to the initial temperature rise was used:

$$SAR = \left(\frac{\Delta T}{\Delta t}\right)_i \cdot \frac{C_w m_w + C_p m_p}{m_p} \qquad (1)$$

where T is the change in temperature in units of K or °C in time t [s] over some interval i. $C_w = 4190\ J\,kg^{-1}\ K^{-1}$ is the specific heat capacity of water, m_w is the dimensionless relative mass of water in the sample, $C_p = 670\ J\,kg^{-1}\ K^{-1}$ is the specific heat capacity of the magnetic nanoparticle (Maenosono and Saita 2006), and m_p is the dimensionless relative mass of the magnetic nanoparticle. The units of SAR reported herein are $W\,g^{-1}$. The relative masses were calculated from the following absolute values in each phantom vial: a 9.92e^{-5} kg water mass and 1.06e^{-6} kg tracer mass.

3. Results

3.1. Quantification of Spatial Localization of Heating

Fig. 5 shows 1D simulation and experimental MPI-MFH results. In Fig. 5(a), simulations of an MFH theoretical model including a spatial gradient field component are provided for $f_0 = 353\ kHz$ and at gradient strengths of 2.35, 4, and 7 $T\,m^{-1}$. Qualitative agreement between the simulated SAR PSF and experimental SAR data were obtained by modeling an 8 nm dextran shell surrounding the 19 nm core. The predicted SAR FWHM for a thermal point source using a 2.35 $T\,m^{-1}$ gradient is approximately 10 mm.

Fig. 5(b) shows experimental SAR and initial rate-of-change temperature data as a function of position for a single vial phantom and a PBS control using the MPI-MFH system. Data was recorded for excitation across a 2 cm FOV in steps of 1 mm with three trials per location. MFH was applied for 10 seconds at each location. A peak SAR deposition of about 150 $W\,g^{-1}$ and a rate of temperature change just under 0.4 $°C\,s^{-1}$ were observed when the sample was coincident with the center of the FFL. The SAR full-width-at-half-maximum (FWHM) is approximately 7.5 mm.

Fig. 5(c) plots experimental SAR and MPI signal using the MPI-MFH system to scan a single vial sample. These data were obtained using the MPI-MFH device at $f_0 = 353$ kHz and 20 mT excitation as in all other heating scans. The MPI signal from the MPI-MFH system is reported as the baseline subtracted magnitude of the 3rd harmonic of the excitation frequency in the time domain data associated with the discrete mean locations of the FFL per the MPI-MFH trajectory. Both data sets are normalized to their peak values for comparison.

Fig. 5(d) plots a 1D PSF of one of the sample vials constructed from data taken with the AWR. The PSF FWHM is approximately 3 mm and was taken using a lower 2 mT excitation amplitude at 353 kHz, in contrast to the 20 mT excitation used in the MPI-MFH device.

3.2. Selective Heating and Imaging of a Phantom

Fig. 6 shows MPI and MPI-MFH data using a triple-vial phantom constructed with the sample vials in Fig. 4(d). The phantom vials were 3 mm apart from each other (7 mm center-to-center distance). Fig. 6(a) shows the phantom imaged at 20 kHz and 20 mT excitation using the FFP scanner of Fig. 4(b). Data acquisition took about 10 minutes and a maximum intensity projection is shown.

Fig. 6(b,c) show data using the MPI-MFH system to individually target each of the three vials of the phantom for heating in separate trials. Fig. 6(b) shows temperature data from individual trials. In all cases, the vial that was targeted rose in temperature significantly, around $0.3 - 0.4 \,^{\circ}C\,s^{-1}$, while the other vials showed little or no rise. As indicated in Fig. 6(b), actuation was performed for an initial 30 second period during which a total temperature increase of $10 - 15 \,^{\circ}C$ was observed in the targeted vial each time. After termination of the AC excitation, heating ceased. Total temperature increases in non-targeted vials was in the range of $0 - 2.5 \,^{\circ}C$. generally less than $1 \,^{\circ}C$.

Fig. 6(c) shows temperature and SAR data quantified and with statistical standard deviation reported for all 5 trials associated with the targeting of each of the 3 vials. The rates of heating of the targeted vials are similar to the SAR experiments of Fig. 5(b), in the range of $130 - 170 \, W\,g^{-1}$ and ($\partial T/\partial t$)$_j$ in the range of $0.3 - 0.4 \,^{\circ}C\,s^{-1}$.

Fig. 7 shows the use of a longer MPI-MFH scanning sequence targeting each of the three vials sequentially for 60 seconds along with the resulting temperature data. Each vial was heated approximately $20 \,^{\circ}C$ over a 60 second actuation period.

4. Discussion

4.1. MFH Localization

In this work, we explored the use of magnetic gradient fields to localize SAR heating. Fig. 5 and Fig. 6 show data that quantify localized heating and demonstrate that SAR spatial resolution can be modeled, with a strong dependence on the strength of the gradient field. Although the nanoMag-MIP particles are polydisperse and have a mixed Brownian and Neel character in terms of magnetic relaxation, the simulation results with our method qualitatively agree with the experimental data. In the future, simulations may be valuable as a pre-planning tool in MPI-MFH therapeutic applications.

The shape of the simulated SAR profiles is very similar to that of the 1D experimental MPI PSF (Langevin-derivative or Lorentzian-like), which is expected given that the same nonlinear saturation physics mediate both MPI and MFH. The shape of the experimental SAR, however, is more rounded. This is also to be expected because the 2 mm-wide vials used in the experimental phantom are not good approximations of point sources. For both the simulated SAR and 1D MPI PSF data, however, a point source was assumed and realized, respectively.

The measured FWHM for the SAR deposition data is about 7.5 mm, and because the sample vial is 2 mm wide, we estimate a heating FWHM of approximately 5.5 mm. The phantom experiments shown in Fig. 6 provide a direct empirical measure of the available thermal resolution in MPI-MFH. When targeting the center vial of the triple-vial phantom, with each vial placed 3 mm away from the adjacent vials, there was modest heating of one of the adjacent vials, indicating we are nearing the thermal resolution limit. In that specific case, the adjacent vial rose in temperature by about $2 \,^{\circ}C$ during the 30 second actuation, while the the targeted vial rose over $10 \,^{\circ}C$. The data also shows that, when actuating a vial at an end of the phantom, the vial at the other end (10 mm away, 14 mm center-to-center) does not heat.

This data confirms our estimate of approximately a 5.5 mm thermal resolution. If we extrapolate from a 2.35 $T\,m^{-1}$ gradient to the 7 $T\,m^{-1}$ gradient in our FFP MPI scanner, we estimate a SAR FWHM of 1.8 mm. In the context of future clinical therapies, a "thermal resolution" in the range of 5.5 mm, as demonstrated in this work, should be more than adequate to avoid heating sites such as the liver while targeting various lesions. If electromagnet gradients are used, the gradient strength can be increased when higher thermal resolution is needed and decreased when spatial separation is large. Lower gradients will allow for more efficient heating of larger lesions.

We believe that the consistently higher heating of vial 3 when compared to vials 1 and 2 (approximately 30%) in the experiments in Fig. 6 are primarily due to the sensitivity of alignment that comes with MPI-based spatial localization in MPI-MFH. In general, there is a tradeoff between thermal resolution and alignment sensitivity (as well as heating efficiency) due to the spatial localizing effect of the FFR. In these data, there were degrees of freedom in both the x and z axes. Imperfect FFL-vial alignment in either or both axes will lead to less than ideal heating of the vial, and this was observed in initial experimentation. Possible sources of relative misalignment include imperfect shift trajectories in z and imperfect vial positioning or tilt in the phantom, a possible confound in both the x and z axes. In general, this motivates the use of a combined MPI-MFH system capable of parallel or simultaneous and real-time imaging to ensure proper alignment during therapy. This is especially true for high gradient and therefore high resolution localized MFH. Differing heat transfer conditions, thermal probe placement in the vial fluid, and minor pipetting differences during sample creation could also have contributed to the observed variation.

For MFH actuation of duration on the order of $10 - 30$ s, as performed in Fig. 5 and Fig. 6, control vials containing PBS show essentially no heating and confirm that Joule heating in the transmit coil system and subsequent conduction or convection heat transfer is not responsible for the heating observed within the tracer vials. However, in Fig. 7, we note heating in the PBS control vial beginning at 150 s. This is due to the hardware limitations of the setup which eventually leads to heat transfer from the Tx coil and/or thermal cross-talk between the neighboring vials.

The small standard deviations in our experimental heating data show that the system performs consistently. While the sequentially actuated data shown in Fig. 7 represents a basic MPI-MFH sequence, it foreshadows how precise x-space trajectories may be leveraged in this theranostics platform.

4.2. Simultaneous MPI-MFH

The 1D MPI PSF data of Fig. 5(d) was taken with a tabletop AWR at the same frequency f_0 = 353 kHz as the MPI-MFH system but at an amplitude of 2 mT. A 2 mT excitation amplitude was used due to power limitations with the device but is also relevant because it represents how one might seamlessly mode switch between heating and imaging with this platform. At 2 mT, detectable macroscopic heating is generally not possible even with high tracer concentrations because of the two orders of magnitude reduction in heating compared to MFH at 20 mT. Thus dialing up and down the excitation amplitude, in addition to varying

FFR trajectories, represents a simple and seamless way of switching between heating and imaging modes.

The narrower shape of the MPI PSF compared to the SAR data could be due to some fundamental differences between the two types of data but may also be explained by the large difference in excitation amplitude. We have demonstrated a strong dependence of the MPI PSF FWHM on the excitation amplitude in the past (Croft et al. 2016) due to the impact of magnetic relaxation, changing slew rates, and the differing size of the partial FOV covered by each oscillation of the excitation field. In general, smaller amplitudes lead to higher resolution with all other variables being constant (ibid.). We therefore posit that changing the experimental drive field from 2 to 20 mT would likewise result in broader MPI PSFs, but this experiment is outside the hardware capabilities of the AWR. Improved MPI capabilities of the combined MPI-MFH device in the future will allow for this analysis directly. It may also be of interest to explore if the shape of the SAR deposition changes analogously with changing excitation amplitude, independent of magnitude scaling.

The 3rd harmonic MPI signal from the MPI-MFH device shown in Fig. 5(c), taken while applying a scanning heating sequence to a single vial, is a proof-of-concept demonstration of simultaneous MPI-MFH. These data align qualitatively well with the SAR data and suggest real-time SAR quantitation via the MPI signal may be obtained in a straightforward manner. These data are an important first step en route to using real-time, quantitative feedback in MPI-MFH.

4.3. MNP Concentrations in Relation to Clinical Applications

In the literature, a "moderate" concentration for clinical MFH of 5 $mg\ mL^{-1}$ has been reported (Jordan, P Wust, et al. 2009), and in one clinical MFH pilot study, we calculated that a prostate tissue MNP concentration of up to 30 $mg\ mL^{-1}$ was established during the therapy (M Johannsen et al. 2005). In comparison, a MNP concentration of 10.6 $mg\ mL^{-1}$ was used in this work, which fits within this range of clinical MFH concentrations. Using this concentration, we showed a repeated ability to achieve a 10–15 $^{\circ}C$ temperature rise within 30 seconds. Given these results, we believe heating up to and beyond the 43 $^{\circ}C$ desired in ablation applications is possible with this approach in an *in vivo* clinical setting. However, active blood perfusion will reduce achievable heating rates in this context. Potentially much lower concentrations could be used in MPI-MFH applications where only mild hyperthermia therapy is desired or in applications where no macroscopic temperature change is required (*e.g.*, drug delivery applications).

We can also compare the MNP concentration used in this work to clinical intravenous iron therapy, as relevant for systemically introduced tracer in diagnostic MPI and MPI-MFH. A 2010 study reported on the safety of Ferumoxytol iron therapy introduced systemically by intravenous injection (M. Lu et al. 2010). The Ferumoxytol was administered as two 510 mg injections separated by 3 – 8 days. If we consider direct injection into a 35 mL target lesion, as in a prostate treated in the previously mentioned MFH clinical pilot study, then the 10.6 $mg\ mL^{-1}$ concentration used in this work would be equivalent to approximately 371 mg of total iron.

We conclude that the use of MNPs in this work is within the clinically relevant range, both in terms of concentration for MFH therapy and total mass in systemic delivery. However, future studies should elaborate on these and other clinical concerns.

5. Conclusions and Future Work

Here we have described the theoretical foundation, physical construction, and testing of an MPI-MFH theranostics platform. We showed that the SAR predicted by theoretical models agrees well with experimental data and may be the basis of future treatment planning optimization strategies. We showed the first experimental data using MPI gradients to deliver targeted heating on demand to components of a phantom with an ability to selectively heat targets separated by as little as 3 mm. We also showed the ability to serially target the component vials using an MPI-MFH sequential scanning sequence. We demonstrated that MPI imaging still works at the high frequencies used in MFH through the use of the AWR. Last, we demonstrated simultaneous MPI-MFH by measuring the MPI signal when using the MPI-MFH device in a heating scan applied to a single vial phantom. Together, these data represent an important step in the development of a theranostics platform for combined MPI-MFH.

Work on combining MPI and MFH has just begun, and we expect development to accelerate in the coming years. An important next step is to explore combined MPI-MFH with *in vivo* applications work such as targeted cancer therapy. Exploring novel therapeutic approaches that do not require macroscopic temperature changes, such as activation of lysosomal pathways and thermal drug delivery, are also of great interest.

Acknowledgments

References

Bauer, Lisa M., et al. High-performance iron oxide nanoparticles for magnetic particle imaging–guided hyperthermia (hMPI). Nanoscale. 2016

Behrends, Andre, et al. Magnetic Particle Spectrometer for the Analysis of Magnetic Particle Heating Applications. International Workshop on Magnetic Particle Imaging. 2016:47.

Borgert, Jörn, et al. Fundamentals and applications of magnetic particle imaging. Journal of cardiovascular computed tomography. 2012; 6(3):149–153. [PubMed: 22682260]

Branquinho, Luis C., et al. Effect of magnetic dipolar interactions on nanoparticle heating efficiency: Implications for cancer hyperthermia. Scientific reports. 2013; 3:2887. [PubMed: 24096272]

Creixell, Mar, et al. EGFR-targeted magnetic nanoparticle heaters kill cancer cells without a perceptible temperature rise. Acs Nano. 2011; 5(9):7124–7129. [PubMed: 21838221]

Croft, Laura R., et al. Low drive field amplitude for improved image resolution in magnetic particle imaging. Medical physics. 2016; 43(1):424–435. [PubMed: 26745935]

Dewey, William C. Arrhenius relationships from the molecule and cell to the clinic. International journal of hyperthermia. 2009; 25(1):3–20. [PubMed: 19219695]

Dewhirst MW, et al. Basic principles of thermal dosimetry and thermal thresholds for tissue damage from hyperthermia. International Journal of Hyperthermia. 2003; 19(3):267–294. [PubMed: 12745972]

Dhavalikar, Rohan, et al. Theoretical predictions for spatially-focused heating of magnetic nanoparticles guided by magnetic particle imaging field gradients. Journal of Magnetism and Magnetic Materials. 2016; 419:267–273. [PubMed: 28943706]

Domenech, Maribella, et al. Lysosomal membrane permeabilization by targeted magnetic nanoparticles in alternating magnetic fields. ACS nano. 2013; 7(6):5091–5101. [PubMed: 23705969]

Eberbeck, Dietmar, et al. Multicore magnetic nanoparticles for magnetic particle imaging. IEEE Transactions on Magnetics. 2013; 49(1):269–274.

Etzioni, Ruth, et al. The case for early detection. Nature Reviews Cancer. 2003; 3(4):243–252. [PubMed: 12671663]

Fan, Qiyong, et al. Emission guided radiation therapy for lung and prostate cancers: A feasibility study on a digital patient. Medical physics. 2012; 39(11):7140–7152. [PubMed: 23127105]

Gleich, Bernhard, et al. Tomographic imaging using the nonlinear response of magnetic particles. Nature. 2005; 435:1214–1217. ISSN: 7046. URL: http://dx.doi.org/10.1038/nature03808. DOI: 10.1038/nature03808 [PubMed: 15988521]

Gleich B, et al. Experimental results on fast 2D-encoded magnetic particle imaging. Physics in medicine and biology. 2008; 53(6):N81. [PubMed: 18367783]

Goodwill, Patrick W., Konkle, Justin J., et al. Projection x-space magnetic particle imaging. IEEE transactions on medical imaging. 2012; 31(5):1076–1085. [PubMed: 22552332]

Goodwill, Patrick W., et al. The X-space formulation of the magnetic particle imaging process: 1-D signal, resolution, bandwidth, SNR, SAR, and magnetostimulation. IEEE transactions on medical imaging. 2010; 29(11):1851–1859. [PubMed: 20529726]

Goodwill, Patrick W., et al. Multidimensional x-space magnetic particle imaging. IEEE transactions on medical imaging. 2011; 30(9):1581–1590. [PubMed: 21402508]

Hilger, Ingrid, et al. Thermal ablation of tumors using magnetic nanoparticles: an in vivo feasibility study. Investigative radiology. 2002; 37(10):580–586. [PubMed: 12352168]

James, Michelle L., et al. A Molecular Imaging Primer: Modalities, Imaging Agents, and Applications. Physiological Reviews. 2012; 92(2):897–965. ISSN: 0031-9333. eprint: http://physrev.physiology.org/content/92/2/897.full.pdf. URL: http://physrev.physiology.org/content/92/2/897. DOI: 10.1152/physrev.00049.2010 [PubMed: 22535898]

Johannsen, Manfred, et al. Magnetic nanoparticle hyperthermia for prostate cancer. International Journal of Hyperthermia. 2010; 26(8):790–795. [PubMed: 20653418]

Johannsen M, et al. Clinical hyperthermia of prostate cancer using magnetic nanoparticles: presentation of a new interstitial technique. International journal of hyperthermia. 2005; 21(7): 637–647. [PubMed: 16304715]

Jordan, Andreas, Scholz, Regina, Maier-Hauff, Klaus, et al. The effect of thermotherapy using magnetic nanoparticles on rat malignant glioma. Journal of neuro-oncology. 2006; 78(1):7–14. [PubMed: 16314937]

Jordan, Andreas, Scholz, Regina, Wust, Peter, et al. Magnetic fluid hyperthermia (MFH): Cancer treatment with AC magnetic field induced excitation of biocompatible superparamagnetic nanoparticles. Journal of Magnetism and Magnetic Materials. 1999; 201(1):413–419.

Jordan, Andreas, Wust, P., et al. Inductive heating of ferrimagnetic particles and magnetic fluids: physical evaluation of their potential for hyperthermia. International Journal of Hyperthermia. 2009; 25(7):499–511. [PubMed: 19848612]

Khandhar, Amit P., et al. Tailored magnetic nanoparticles for optimizing magnetic fluid hyperthermia. Journal of Biomedical Materials Research Part A. 2012; 100(3):728–737. [PubMed: 22213652]

Konkle, Justin J., Goodwill, Patrick W., Carrasco-Zevallos, Oscar M., et al. Projection reconstruction magnetic particle imaging. IEEE transactions on medical imaging. 2013; 32(2):338–347. [PubMed: 23193308]

Konkle, Justin J., Goodwill, Patrick W., Hensley, Daniel W., et al. A convex formulation for magnetic particle imaging x-space reconstruction. PloS one. 2015; 10(10):e0140137. [PubMed: 26495839]

Kuboyabu, Tomomi, et al. Usefulness of Magnetic Particle Imaging for Monitoring the Effect of Magnetic Targeting. Open Journal of Medical Imaging. 2016; 6(02):33.

Kumar, Challa SSR., et al. Magnetic nanomaterials for hyperthermia-based therapy and controlled drug delivery. Advanced drug delivery reviews. 2011; 63(9):789–808. [PubMed: 21447363]

Laurent, Sophie, et al. Magnetic fluid hyperthermia: focus on superparamagnetic iron oxide nanoparticles. Advances in colloid and interface science. 2011; 166(1):8–23. [PubMed: 21601820]

Li, Chun. A targeted approach to cancer imaging and therapy. Nature materials. 2014; 13(2):110–115. [PubMed: 24452345]

Lu, Kuan, et al. Linearity and shift invariance for quantitative magnetic particle imaging. IEEE transactions on medical imaging. 2013; 32(9):1565–1575. [PubMed: 23568496]

Lu, Min, et al. FDA report: ferumoxytol for intravenous iron therapy in adult patients with chronic kidney disease. American journal of hematology. 2010; 85(5):315–319. [PubMed: 20201089]

Maenosono, Shinya, et al. Theoretical assessment of FePt nanoparticles as heating elements for magnetic hyperthermia. IEEE transactions on magnetics. 2006; 42(6):1638–1642.

Maier-Hauff, Klaus, et al. Efficacy and safety of intratumoral thermotherapy using magnetic iron-oxide nanoparticles combined with external beam radiotherapy on patients with recurrent glioblastoma multiforme. Journal of neuro-oncology. 2011; 103(2):317–324. [PubMed: 20845061]

Martsenyuk MA, et al. On the kinetics of magnetization of ferromagnetic particle suspensions. Sov Phys JETP. 1974; 38:413.

Maruyama S, et al. Development of Magnetic Nanocarriers based on Thermosensitive Liposomes and their Visualization using Magnetic Particle Imaging. Int J Nanomed Nanosurg. 2016; 2(2)

Murase, Kenya, Aoki, Marina, et al. Usefulness of Magnetic Particle Imaging for Predicting the Therapeutic Effect of Magnetic Hyperthermia. Open Journal of Medical Imaging. 2015; 5(02):85.

Murase, Kenya, Takata, Hiroshige, et al. Control of the temperature rise in magnetic hyperthermia with use of an external static magnetic field. Physica Medica. 2013; 29(6):624–630. [PubMed: 22985766]

Narasimha M, et al. Numerical simulation of magnetite segregation in a dense medium cyclone. Minerals Engineering. 2006; 19(10):1034–1047.

Nishimoto, Kohei, et al. Application of magnetic particle imaging to pulmonary imaging using nebulized magnetic nanoparticles. Open Journal of Medical Imaging. 2015; 5(02):49.

Orendorff, Ryan, et al. 2016 World Molecular Imaging Congress (WMIC 2016): Imaging Biology… Improving Therapy. World Molecular Imaging Society (WMIS); 2016. First in vivo Brain Perfusion Imaging using Magnetic Particle Imaging.

Pablico-Lansigan, Michele H., et al. Magnetic particle imaging: advancements and perspectives for real-time in vivo monitoring and image-guided therapy. Nanoscale. 2013; 5(10):4040–4055. [PubMed: 23538400]

Rahmer, Jürgen, et al. Signal encoding in magnetic particle imaging: properties of the system function. BMC medical imaging. 2009; 9(1):1. [PubMed: 19133127]

Rahmer, Jürgen, et al. Analysis of a 3-D system function measured for magnetic particle imaging. IEEE transactions on medical imaging. 2012; 31(6):1289–1299. [PubMed: 22361663]

Rosensweig, Ronald E. Heating magnetic fluid with alternating magnetic field. Journal of magnetism and magnetic materials. 2002; 252:370–374.

Rosensweig, Ronald E. Ferrohydrodynamics. Courier Corporation; 2013.

Sapareto, Stephen A., et al. Thermal dose determination in cancer therapy. International Journal of Radiation Oncology* Biology* Physics. 1984; 10(6):787–800.

Saritas, Emine U., et al. Magnetic particle imaging (MPI) for NMR and MRI researchers. Journal of Magnetic Resonance. 2013; 229:116–126. [PubMed: 23305842]

Serres, Sébastien, et al. Molecular MRI enables early and sensitive detection of brain metastases. Proceedings of the National Academy of Sciences. 2012; 109(17):6674–6679.

Tasci, T Onur, et al. Focused RF hyperthermia using magnetic fluids. Medical physics. 2009; 36(5): 1906–1912. [PubMed: 19544810]

Tay, Zhi Wei, et al. A High-Throughput, Arbitrary-Waveform, MPI Spectrometer and Relaxometer for Comprehensive Magnetic Particle Optimization and Characterization. Scientific reports. 2016; 6

Thiesen, Burghard, et al. Clinical applications of magnetic nanoparticles for hyperthermia. International Journal of Hyperthermia. 2008; 24(6):467–474. eprint: http://dx.doi.org/

10.1080/02656730802104757. URL: http://dx.doi.org/10.1080/02656730802104757. DOI: 10.1080/02656730802104757 [PubMed: 18608593]

Torres-Lugo, Madeline, et al. Thermal potentiation of chemotherapy by magnetic nanoparticles. Nanomedicine. 2013; 8(10):1689–1707. [PubMed: 24074390]

Weaver, John B., et al. Magnetic nanoparticle temperature estimation. Medical physics. 2009; 36(5): 1822–1829. [PubMed: 19544801]

Weizenecker J, et al. Three-dimensional real-time in vivo magnetic particle imaging. Physics in medicine and biology. 2009; 54(5):L1. [PubMed: 19204385]

Wilhelm, Stefan, et al. Analysis of nanoparticle delivery to tumours. Nature Reviews Materials. 2016; 1:16014.

Yu, Elaine, et al. 2016 World Molecular Imaging Congress (WMIC 2016): Imaging Biology… Improving Therapy. World Molecular Imaging Society (WMIS); 2016. First demonstration of in vivo Cancer Magnetic Particle Imaging with IV-administered Passive Long-circulating SPIOs.

Zhang J, et al. Magnetic drug-targeting carrier encapsulated with thermosensitive smart polymer: core–shell nanoparticle carrier and drug release response. Acta Biomaterialia. 2007; 3(6):838–850. [PubMed: 17638599]

Zheng, Bo, von See, Marc P., et al. Quantitative Magnetic Particle Imaging Monitors the Transplantation, Biodistribution, and Clearance of Stem Cells In Vivo. Theranostics. 2016; 6:291–301. ISSN: 3. URL: http://www.ncbi.nlm.nih.gov/pmc/articles/PMC4737718/. DOI: 10.7150/thno. 13728 [PubMed: 26909106]

Zheng, Bo, Vazin, Tandis, et al. Magnetic Particle Imaging tracks the long-term fate of in vivo neural cell implants with high image contrast. Scientific reports. 2015; 5

Zhou, Xinyi, et al. 2016 World Molecular Imaging Congress (WMIC 2016): Imaging Biology… Improving Therapy. World Molecular Imaging Society (WMIS); 2016. In Vivo Magnetic Particle Imaging of Lung Perfusion in Rats - Towards High Sensitivity and High Contrast Non-Radiation Based Diagnostics for Pulmonary Embolism.
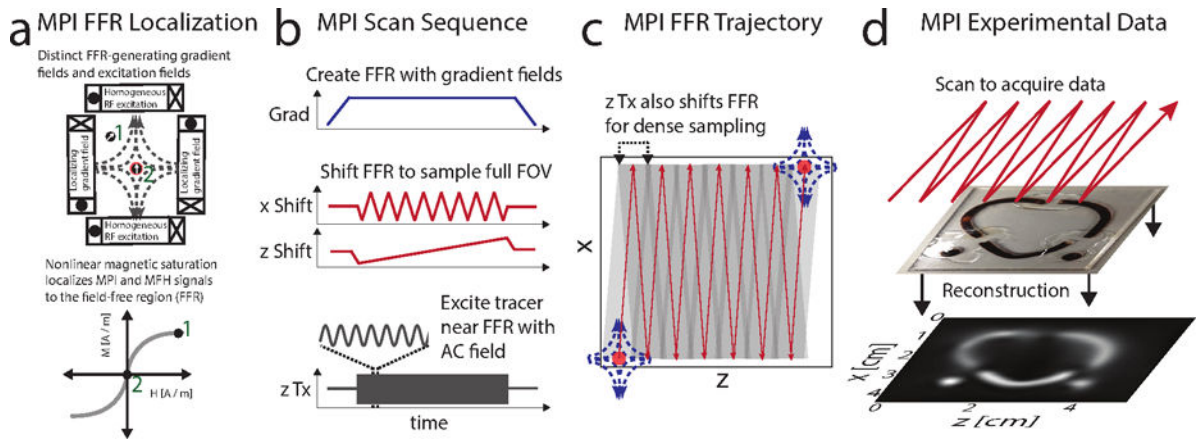
Figure 1.
FFR localization and magnetic particle imaging, (a) Depiction of a field-free region (FFR), created by opposing magnets, and separate homogeneous excitation magnets. Only tracer at position 2 located near the FFR is unsaturated and capable of producing an appreciable MPI or MFH signal when exposed to an AC field. (b,c) During an MPI scan, gradient waveforms create the FFR, shift waveforms move the mean location of the FFR to cover the entire field-of-view (FOV), and an AC (transmit or Tx) waveform provides the temporally fast excitation. The superposition of shift and excitation waveforms provides an overlapping and dense sampling of the FOV. (d) MPI experimental results for a single slice from a 10 minute tomographic scan of a simple phantom using a Berkeley scanner. In reconstruction, the received time-domain data is correlated with the trajectory of the FFR in the image domain to grid images.
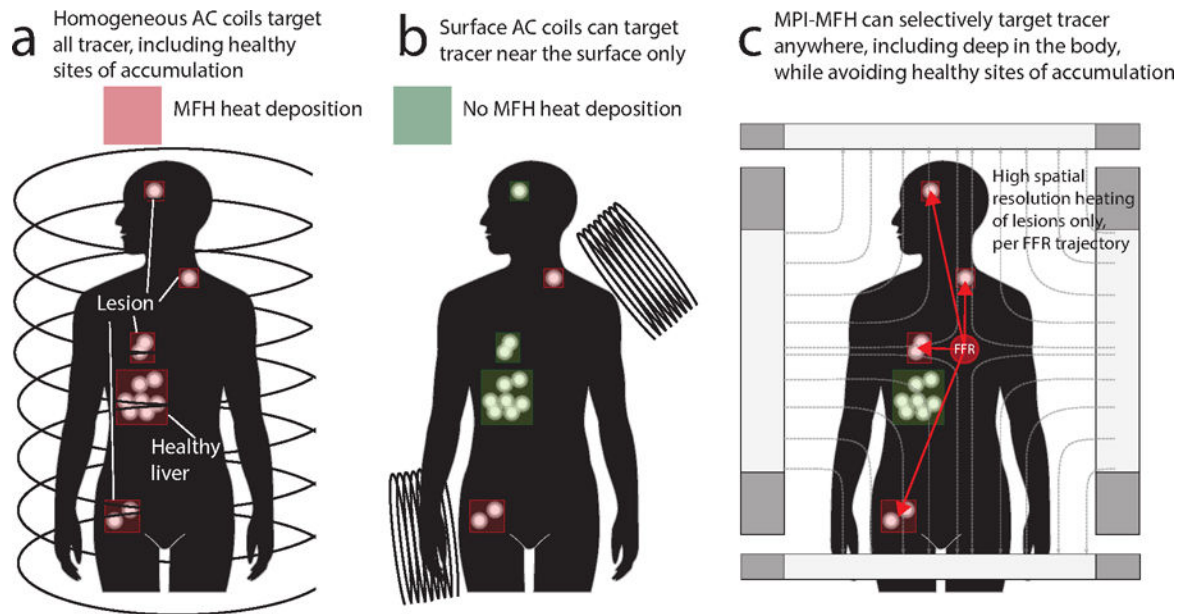
Figure 2.
Localizing magnetic fluid hyperthermia, (a) Homogeneous AC coil designs apply therapy to all locations where the SPIOs have accumulated, including healthy sites, (b) Surface AC coils can be used to target sites of accumulation near the surface of the subject but not sites deep in the body, (c) MPI-MFH as proposed here can target any site desired using the FFR, including those deep in the body, with high resolution. Healthy sites of accumulation can be avoided.
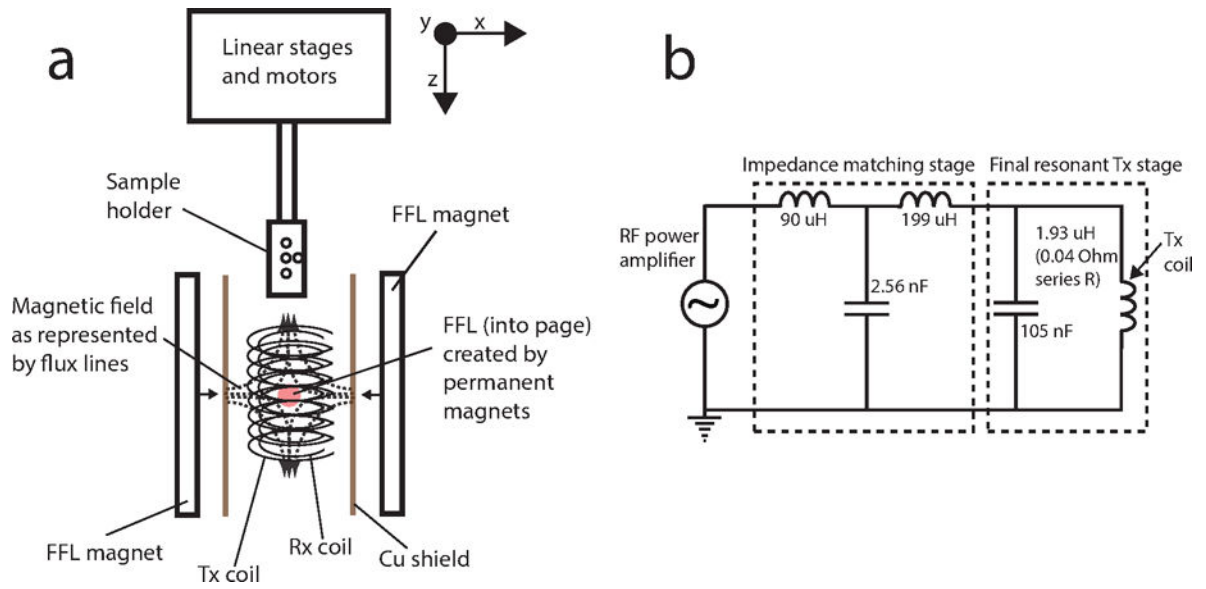
Figure 3.
MPI-MFH system diagrams. (a) Diagram of the major structural components: permanent magnet array for creation of a field-free line (FFL), imaging bore with concentric transmit excitation (Tx) and MPI receive (Rx) coils, and sample movement system with linear stages and motors, (b) Circuit diagram for the 353 kHz resonant transmit (Tx) chain with major components: impedance matching and low pass filter, final resonant Tx stage, and Tx coil.
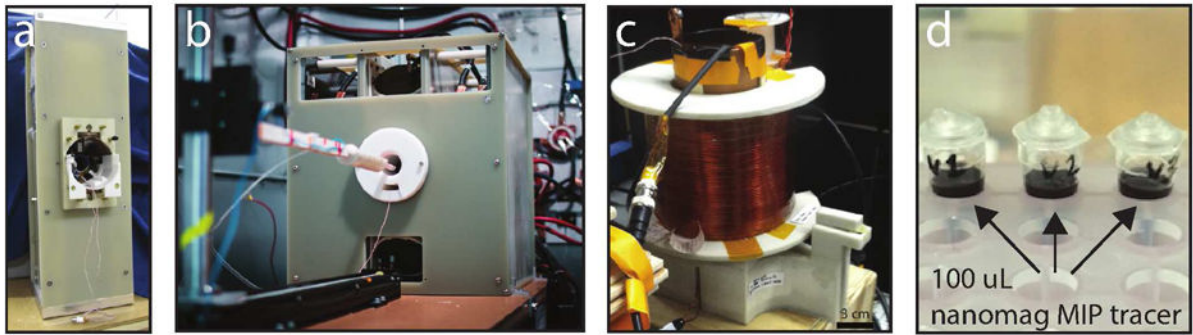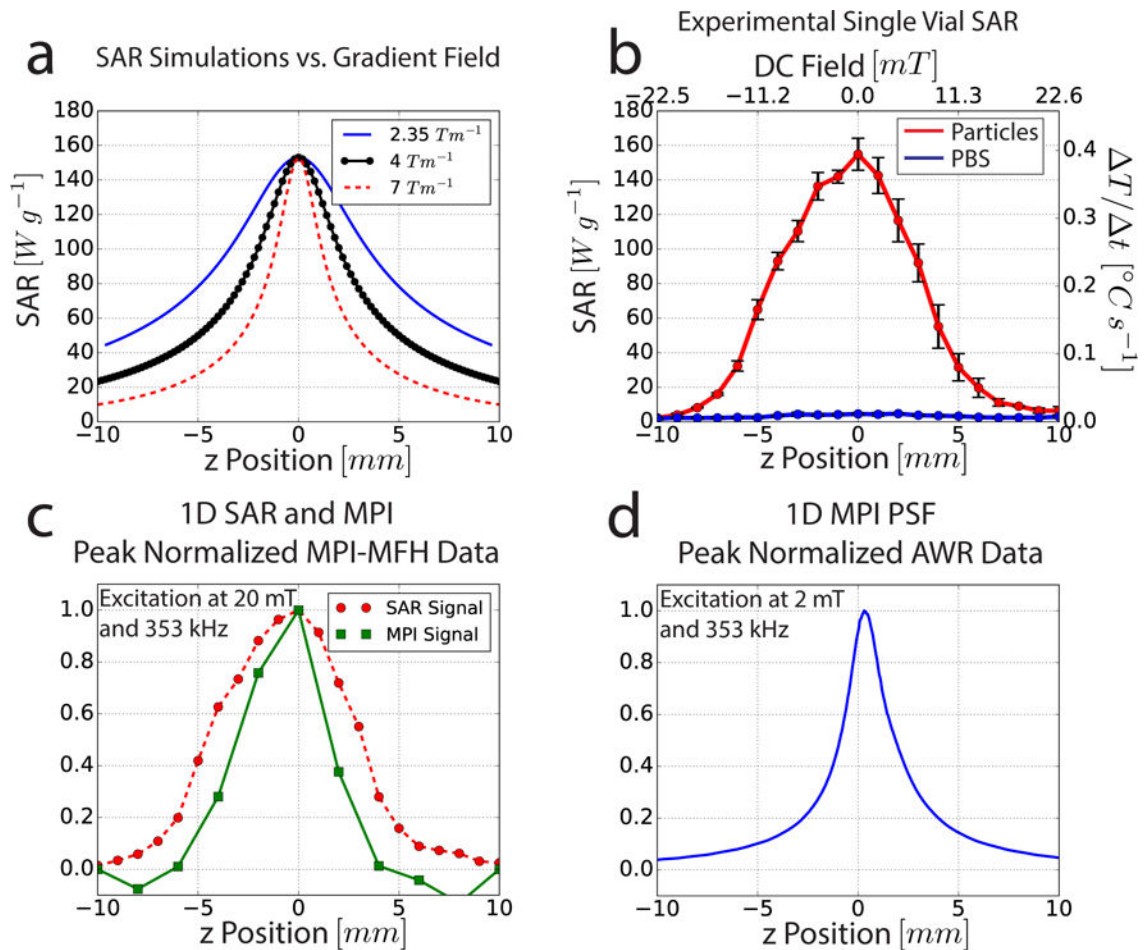
Figure 4.
Hardware systems and vial phantoms used in this work, (a) Combined MPI-MFH system, (b) FFP scanning system used for multi-dimensional imaging. This system produces a $3.5 \times 3.5 \times 7$ [Tm^{-1}] gradient field with excitation at 20 kHz. (c) Arbitrary waveform relaxometer (AWR) table top MPI characterization system with no gradients. The AWR is capable of characterizing the ID MPI PSF for a sample over a wide range of frequencies and field amplitudes, (d) Vial samples used in phantoms. 100 uL of nanoMag MIP magnetic nanoparticles were placed in small PCR tubes.

Figure 5.
Spatial localization of heating with MPI-MFH in 1D. (a) Simulations of specific absorption rate (SAR) for the SPIOs used in this work at various gradient fields. (b) Experimental SAR data using the MPI-MFH system and applied to both a single vial with SPIOs and a PBS control. (c) Normalized plots of experimental SAR and experimental MPI signal (magnitude of the 3rd harmonic) from the MPI-MFH system. (d) Experimental 1D MPI PSF from the AWR. All experimental data and simulations use 353 *kHz* excitation.
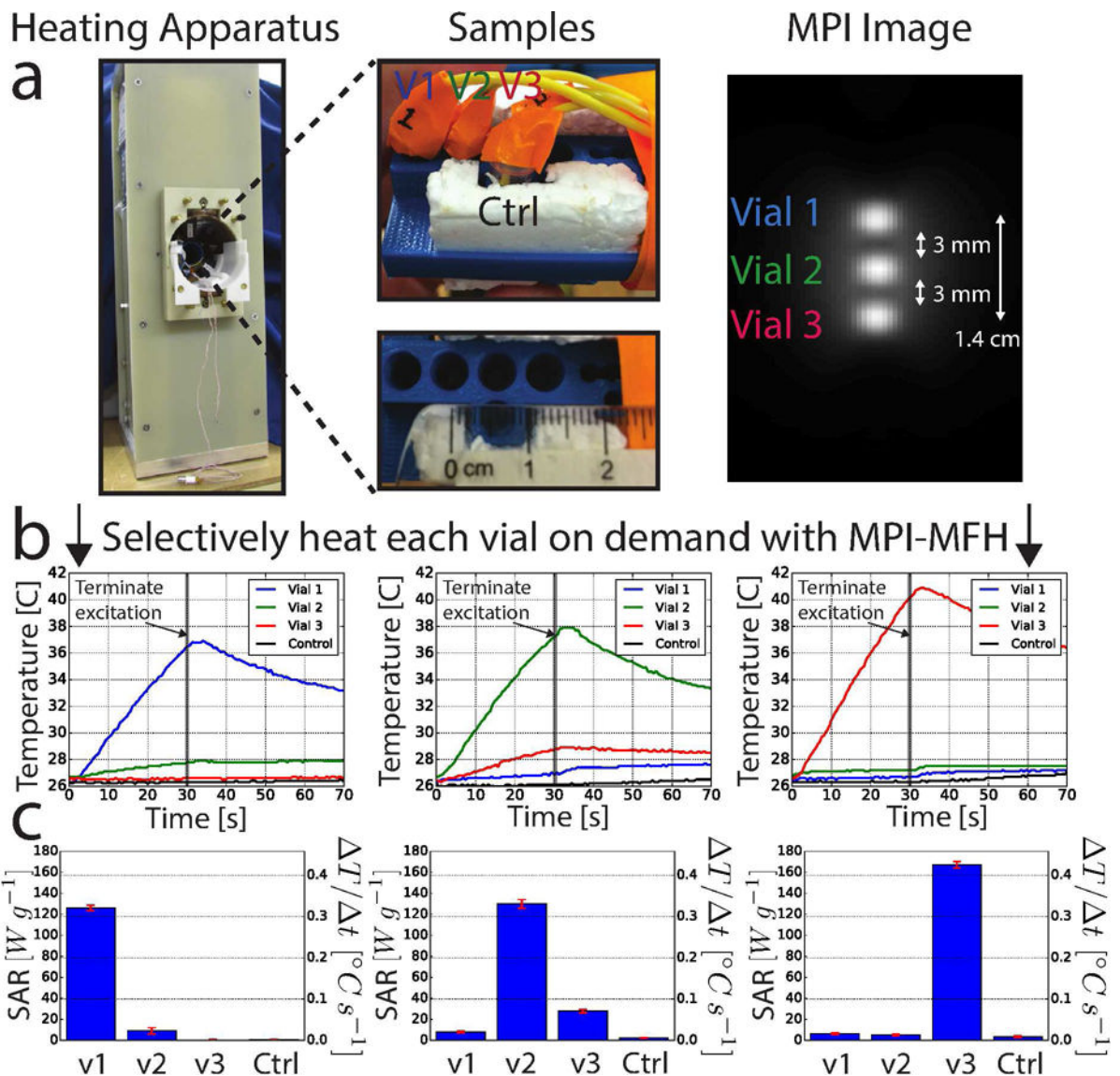
Figure 6.
Selective heating with MPI-MFH. (a) MPI-MFH device, SPIO phantom, and MPI image
taken with a FFP scanner. The phantom vials were 3 mm apart (7 mm center-to-center). (b)
MPI-MFH temperature data for trials when each of the three phantom components was
targeted for individual heating, (c) SAR and temperature data quantified for all 5 trials
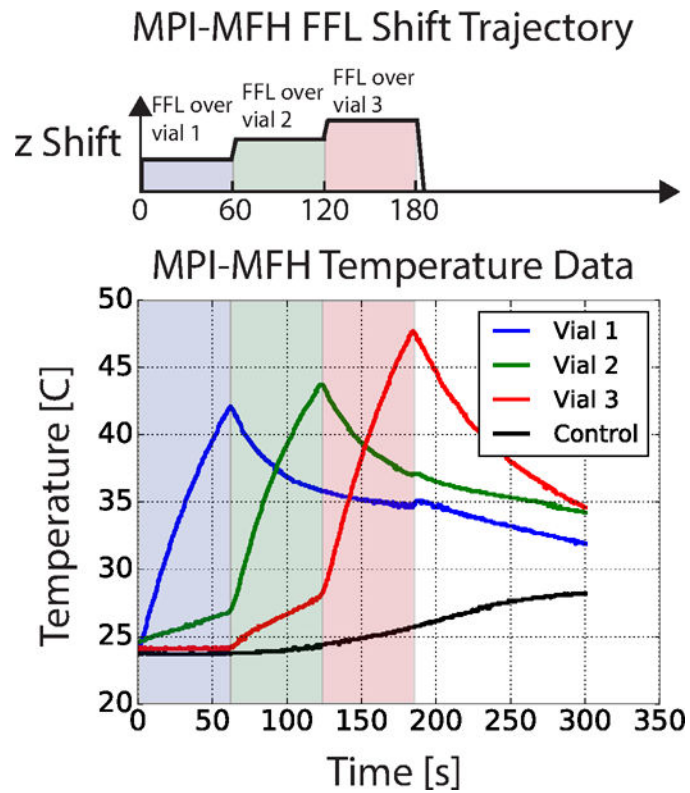associated with targeting each of the 3 phantom vials.

Figure 7.
Implementation of an MPI-MFH scanning sequence to actuate multiple distinct locations in a single therapeutic scan. While AC excitation is applied, the localizing FFL is sequentially aligned with each of the three vials in the phantom to realize temporo-spatially selective heating. The MPI-MFH method provides high resolution, flexible, and dynamically configurable therapeutic targeting.